AIAA 99-3149

Sensing Aircraft Effects by Flap Hinge Moment Measurement

Holly M. Gurbacki and Michael B. Bragg
University of Illinois at Urbana-Champaign
Urbana, IL

17th Applied Aerodynamics Conference

June 29–July 1, 1999

Norfolk, VA

Sensing Aircraft Icing Effects by Flap Hinge Moment Measurement

Holly M. Gurbacki*, Michael B. Bragg†
University of Illinois at Urbana-Champaign

Abstract

Simulated large-droplet ice accretions were tested on a NACA 23012 airfoil with simple flap in the UIUC subsonic wind tunnel. Reduced lift, increased drag, changes in pitching moment and hinge moment were measured due to the ice simulation. These resulted from a separation bubble that formed behind the simulated ice, severely altering the surface pressure distribution. The steady-state hinge moment became nonlinear when flow separation occurred over the flap and was most affected when the simulated ice accretion was located furthest aft on the upper surface. The fluctuation of the flap hinge moment was measured and characterized by a RMS parameter that exhibited a maximum value at or near maximum lift. The current research relates this unsteady parameter to the steady-state aerodynamic coefficients in addition to the flow characteristics associated with the separation bubble. As opposed to the steady-state value, the change in the RMS hinge moment was observed during the linear phase of the lift curve several degrees before stall.

1.0 Introduction

Ice accretion on an airfoil changes the shape and thus the performance characteristics of the airfoil. In some icing conditions an ice ridge can form on the surface of an airfoil leading to reduced lift, increased drag, change in pitching and hinge moments and a loss in control effectiveness. These are often the result of a separation bubble aft of the ice ridge, which affects performance by altering the pressure distribution over the airfoil. The flow separates from the airfoil surface at the location of the ice and either attaches at some distance downstream or completely fails to reattach, resulting in premature airfoil stall. This can result from a steep angle of attack, a large flap deflection or a high ice ridge. In the case of separation on the upper surface, the pressure acting on the surface is reduced. Since the lower surface pressure distribution remains generally unchanged, there is an upward force imposed on the flap that acts to deflect the flap in that direction. The flap is essentially sucked upward by the lower pressure. Due to the increased lift force on the control surface a negative hinge moment also occurs.

This abrupt ice-induced flow separation can lead to a sudden significant change in hinge moment leaving insufficient time for the pilot to react correctly. Such occurrences have led to aircraft accidents in the past. Thus, it is desirable to sense impending problems before they occur, in order to warn the pilot and potentially alter the control system.[1] A better understanding of this phenomenon is required before a reliable means of sensing these changes can be developed.

Trunov and Ingelman-Sundberg[2] demonstrated the effect of ice on the hinge moment of a tailplane. For the clean case, the hinge moment increases linearly with negative angle of attack until rising sharply at stall. The nonlinearity is the result of flow separation from the lower tailplane surface, where the control surface is abruptly sucked downward due to the decreased pressure. In the case of ice or roughness at the leading edge, the break in the linear curve occurs at a smaller, less negative angle, and the hinge moment sharply increases until eventually leveling out after tailplane stall.

Besides performance degradation, separated flow over a control surface can lead to reduced control effectiveness. When the flow no longer follows the contour of the airfoil, flap deflection has little effect on the flow pattern. The pilot's ability to control aircraft motion through the surface device is greatly reduced. This effect was related to icing as far back as 1940 when Johnson[3] measured a 40 percent reduction in roll authority due to the presence of ice.

Problems such as the increased magnitude in hinge moment and the loss of control effectiveness may have led to a number of past ice-related aircraft accidents. It is suspected that the ATR-72 commuter aircraft flight 4184 that crashed on October 31, 1994 in Roselawn, Indiana is one such example. Bragg[4] speculates as to the cause of the incident upon review of the flight recorder data.

---

* Graduate Research Assistant, Department of Aeronautical and Astronautical Engineering, member AIAA.
† Professor and Head, Department of Aeronautical and Astronautical Engineering, Associate Fellow AIAA.

In order to properly react to ice-induced control problems and maintain safety of the aircraft and crew, the pilot must be warned of potential problems before they occur. Several systems under development seek to increase in-flight pilot awareness of icing effects by monitoring, and possibly predicting degraded aerodynamic performance. This is achieved by detecting the presence and extent of separated flow. Flow unsteadiness can be sensed by measurement of surface pressure or velocity fluctuations as a function of time.

One such device is the Aircraft Icing Performance Monitoring System, AIMS. The system was developed to detect flow separation and potential stall on aerodynamic surfaces by non-intrusive sensors that measure pressure fluctuations on the low-pressure side of the wing.[5] Stall Warning Plus stall warning and advisory system is another system that monitors pressure by use of high-frequency solid-state pressure sensors. It senses airfoil contamination by monitoring both the fluctuating and steady components of the local velocity.[6] A third contamination detection product is the System for On-board Lift Analysis / AirSpeed Directional Indicator System, SOLA/ASDIS. It collects time-dependent pressure measurements by an array of differential pressure sensors and uses a non-dimensional parameter to quantify airfoil lift capability.[7]

Each of the systems monitors flow unsteadiness by measuring surface pressure fluctuations. The differences that distinguish the devices depend largely on the instrumentation or type of sensor used to acquire the essential data and the calculated parameter that is used to monitor aerodynamic performance. A slightly different approach is the smart icing system under development at the University of Illinois at Urbana-Champaign,[1] which proposes a system that senses the actual in-flight aircraft performance degradation and further relates this information to the pilot and crew. An Ice Management System (IMS) is created and is integrated into present-day avoidance and ice protection concepts, using traditional icing sensors to detect the presence of ice, and modern system identification methods to estimate changes in performance and control. The system operates based on real-time ice accretion effects and maintains full communication with the flight crew. It is hoped that the research presented in this paper will be further incorporated into the ice accretion sensing mechanism of this overall approach.

Because the unsteady separated flowfield is the cause of the aforementioned hazardous aircraft control problems, the proposed research will also make use of unsteady flow characteristics using another sensing parameter, the unsteady flap hinge moment. In reference to the change in hinge moment with angle of attack for an iced airfoil, it is necessary that the nonlinear behavior (the break in the curve due to ice-induced flow separation) be predicted from data in the linear range. Unsteady hinge moment data will be correlated with the steady-state data in addition to the unsteady flowfield and those conditions leading to the possible loss of aircraft control.

An advantage of using the unsteady hinge moment as an advance indicator of degraded performance and control, as opposed to the parameters used in the previously mentioned systems, is that it measures the integrated effect of ice over the entire area of concern, rather than at only a single point on the surface. Furthermore, it is resistant to operational and environmental wear, whereas a surface sensor may be plugged by ice or damaged by a foreign object.

2.0 Experimental Methods

The tests were performed at the University of Illinois Subsonic Aerodynamics Laboratory in the 3 x 4 foot low-turbulence wind tunnel. The tunnel is a conventional indraft, open-return type that exhausts into the tunnel room. The inlet settling chamber consists of a honeycomb flow straightener and four anti-turbulence screens, and the contraction ratio between the inlet and test section is 7.5:1. Desired airspeed is achieved through a variable frequency drive, which controls a 125 horsepower motor and a five-bladed fan.

The airfoil model was an 18-inch modified NACA 23012 with a 25 percent chord simple flap. In comparison to a conventional 23012 airfoil, the model has a slightly drooped leading edge with a maximum vertical coordinate shift of 0.4 percent chord and a maximum thickness of 12.2 percent. The hinge axis and leading edge of the flap are located at x/c = 0.779 and x/c = 0.75, respectively. 50 surface pressure taps are located on the model main element with an additional 30 taps on the flap, including 12 in the spanwise direction. These were connected to an electronically scanned pressure (ESP) system, which also measured the pressures of the 59 probes in a traversable wake rake.

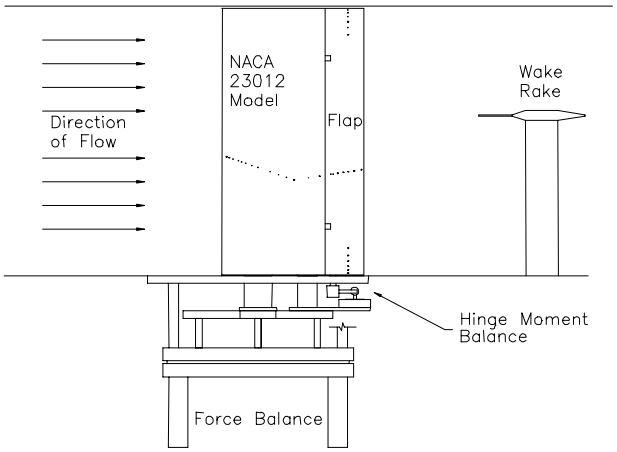

Fig. 1. Schematic of the experimental setup.

Figure 1 shows the schematic of the experimental setup. The model was attached vertically to a three-component force and moment balance, which was also used to set the angle of attack. The flap was actuated by a two-arm linkage system, driven by a linear traverse that was mounted on the metric force plate of the balance. A load cell was attached in one of the arms and measured the flap hinge moment. The flap gap was sealed during the tests with a mylar strip that was sucked up against the lower surface of the model by the lower pressure on the upper surface.

The simulated ice accretion used in the experiment was a forward facing, wooden, quarter round of 0.25-inch radius. The ice accretion was placed on the airfoil model at locations of x/c = 0.02, 0.10 and 0.20. The tests were performed at a maximum Reynolds number of 1.8 million and the varied parameters included angle of attack (α), flap deflection (δ_f) and freestream velocity. A typical run consisted of sweeping the angle of attack from –8° to a few degrees past positive stall in 1° increments, at a given Reynolds number and flap deflection. At each angle of attack, the steady-state lift, drag, and moment about the model quarter-chord were measured, in addition to both the steady and unsteady hinge moments. Reynolds numbers remained at 0.5, 1.0, and 1.8 million, and flap deflection varied in 5° increments from 0° to 15°.

The lift coefficient (C_λ) and pitching moment coefficient (C_m) were calculated from the integrated surface pressure measurements and the drag coefficient (C_d) was calculated from the wake rake data. The flap hinge moment coefficient (C_h) was determined from the flap hinge load cell and the surface pressure distributions were obtained by calculation of the pressure coefficient (C_p) from the measured pressures.

Table 1. Experimental uncertainties for the clean model at $\alpha = 5^o$, Re = 1.8 million.

Aerodynamic Coefficient	Reference Value	Absolute Uncertainty	Relative Uncertainty
C_l Pressure	0.633	2.11×10^{-03}	0.33%
C_d Wake	0.01022	1.43×10^{-04}	1.40%
C_m Pressure	-0.00894	3.49×10^{-04}	3.90%
C_h Balance	-0.0157	3.55×10^{-03}	9.70%

Standard methods with conventional definitions were used to calculate C_λ, C_m, and C_d from the measurements. The C_h was obtained by determining the trailing-edge down moment about the flap hinge line and nondimensionalizing by the flap surface area and the flap chord length. All of the aerodynamic coefficients were corrected for wall effects by using the method described by Rae and Pope.[8]

The steady-state lift, drag, pitching moment and hinge moment measurements were taken at 50 Hz for 2 seconds and then time averaged. The unsteady flap hinge moment measurements were taken at 3000 Hz for angles of attack less than zero degrees, and 2000 Hz for angles of zero degrees or greater. A total of 10,000 samples were taken for each unsteady measurement. The only measurement that was filtered was the force balance data, which was low-pass filtered at 1Hz.

The uncertainty estimates of the aerodynamic coefficients for a typical data point are shown in Table 1. The case shown is that of the clean model at $\alpha = 5^o$ with zero flap deflection and Re = 1.8 million. The relative uncertainties for the C_m and the C_h appear to be rather large, but this was due to relatively small reference values at this point.

The clean model baseline measurements were taken and compared with the previously published experimental measurements of Stuttgart.[9] The Stuttgart data achieved a slightly higher angle of attack at stall but otherwise compared favorably with the current measurements, thus validating the experimental apparatus and data reduction methods of this study.

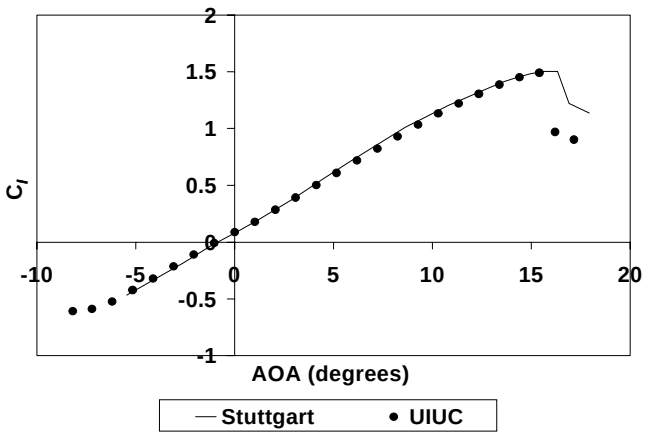

Fig. 2. Comparisons of clean NACA 23012 lift measurements between present UIUC data and Stuttgart.[9] (UIUC Re = 1.8 million; Stuttgart Re = 2.0 million)

3.0 Results and Discussion

3.1 Simulated Ice Effects on C_λ, C_d and C_m

Figure 3 shows the effects of the simulated ice on the steady-state aerodynamic coefficients in comparison to the clean airfoil. The test conditions for the data presented in this section are a Reynolds number of 1.8 million and flap deflection of 0º.

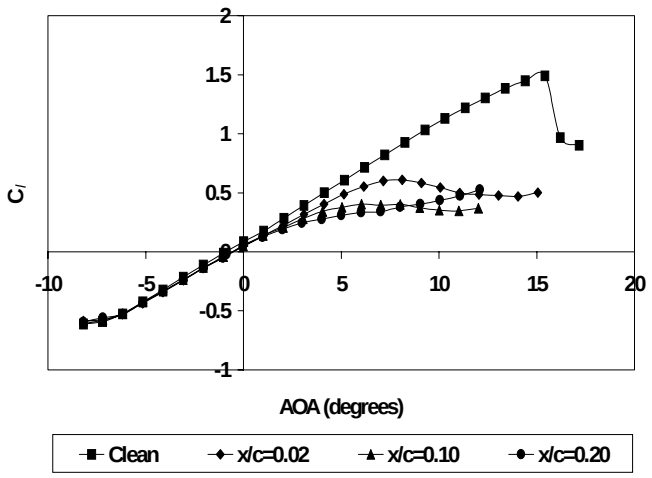

Fig. 3a. Lift curve comparison for different simulated ice shape locations at Re = 1.8 million.

Figure 3a shows the effect of simulated ice on the lift coefficient at three different ice shape locations. The maximum lift coefficient ($C_{\lambda max}$) is significantly reduced and the stall type is affected. For the clean case, a $C_{\lambda max}$ of approximately 1.5 is reached. This is reduced by approximately 60% and 70% for the simulated-iced cases at x/c = 0.02 and x/c = 0.10, respectively. The worst case occurs when the quarter round is placed at x/c = 0.20, with a reduction in $C_{\lambda max}$ of almost 80%. Note that for this case, the lift increases steadily with angle of attack until approaching $\alpha = 6°$, where it levels off before rising again. Although it is difficult to determine an exact value of $C_{\lambda max}$, it is estimated to occur at this angle. An additional result of the simulated-iced flowfield is a 60% reduction in the angle of attack at which stall occurs (α_{stall}).

Table 2. Lift-related quantities at Re = 1.8 million.

Test Case	$C_{l, max}$	α_{stall}	$C_{l\alpha}$
Clean	1.5	15.4°	0.0978
x/c = 0.02	0.6	8°	0.0926
x/c = 0.10	0.4	6°	0.0923
x/c = 0.20	0.3	6°	0.0932

A change in the stall type also results from the presence of the simulated-ice shapes. The sharp stall of the clean airfoil is compared to the gradual bending of the simulated-iced airfoil curve, changing the characteristic leading-edge stall type of the NACA 23012 to that of a thin-airfoil type stall. Furthermore, the lift curve slope in the linear range for the clean case is slightly higher than that for the simulated-iced cases. A list of values for the aforementioned quantities are given in Table 2 for each of the four tested cases.

The effect of the simulated ice on airfoil drag at the three different x/c locations is seen in Figure 3b. There is a significant increase in drag between the clean case and the case of simulated ice at x/c = 0.02 for $C_\lambda > 0$. This increase in drag worsens as the quarter round is moved aft along the upper surface of the airfoil with a trend comparable to that of the decrease in $C_{\lambda max}$. A kink or nonlinearity can also be identified in the simulated-iced cases that will later be compared to the steady and unsteady hinge moment coefficient. The drag of the clean C_d curve is fairly linear until approaching $C_{\lambda max}$ where it abruptly increases in value at stall. For each of the simulated-iced cases, the C_d curves exhibit a similar linear trend that is interrupted by a kink in the curve, leading to a gradual increase in drag.

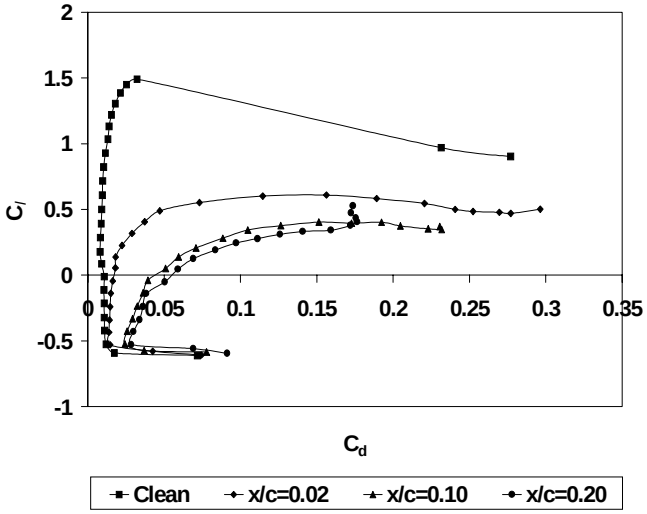

Fig. 3b. Drag comparison for different simulated ice shape locations at Re = 1.8 million.

The change in the pitching moment about the quarter chord position due to the presence of the simulated ice is illustrated in Figure 3c. For the clean airfoil, the C_m breaks at about $\alpha = 16°$. For the simulated-iced cases, the C_m curves break at lower angles that decrease as the quarter round moves from x/c = 0.02 to x/c = 0.20. Furthermore, the negative slope of the curve after the break decreases in a similar manner, with the slope of the clean case being the highest and the slope of the simulated-iced case at x/c = 0.20 being the smallest.

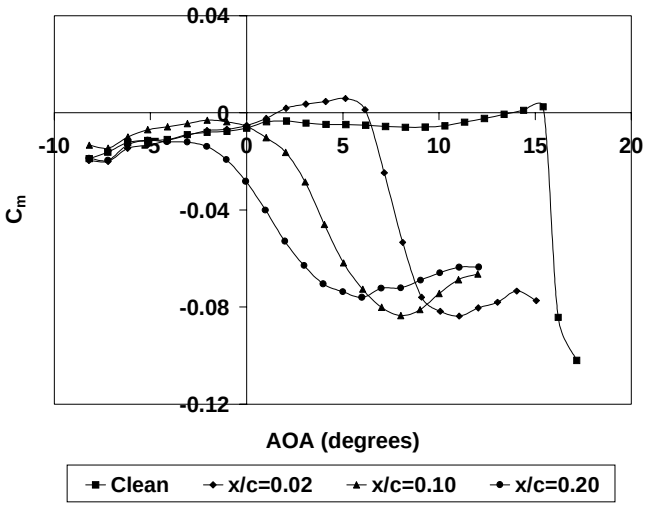

Fig. 3c. Moment about the quarter-chord comparison for different simulated ice shape locations at Re = 1.8 million.

3.2 Simulated Ice Effects on Steady and Unsteady C_h

The steady-state flap hinge moment exhibits a trend similar to that of the pitching moment with regard to the presence of simulated ice. Although in most cases the break in the C_h curve is visibly evident, a calculation was performed to determine the angle of attack at which the slope of the C_h curve changes the most. Second-order forward and backward difference equations were calculated and compared based on the three data points before and after a given point. The percentage difference between the two values was the greatest when there existed a significant change in the slope, corresponding to the break in the C_h curve.

Figure 4 shows that while the clean C_h curve breaks at α = 16°, the C_h curves for the simulated-iced cases break at decreasing angles of attack with increasing x/c position. The rate at which C_h decreases with angle of attack is also a function of the simulated ice location. For the clean case, the rate of decrease is large, resulting in a large negative slope between α = 15° and 16°. This rate decreases as the simulated ice is placed at x/c = 0.02 and moved aft to x/c = 0.10 and 0.20. For these last two cases, there is no significant difference in the rate of decrease. It is also interesting to note that all the curves diverge from the same approximate point at α = -8° and that at negative angles of attack, in the linear portions of the curves, the C_h values increase in magnitude as the simulated ice is moved aft on the airfoil surface.

The effect of flap deflection on the steady-state hinge moment is also illustrated in Figure 4, and is primarily a shift in the C_h curves. A positive change in flap deflection from 0° to 10° results in a negative shift of the C_h values. This reduction of the hinge moment coefficient indicates an increase in lift. Table 3 presents $C_{\lambda max}$ and α_{stall} for the clean case and each of the simulated-iced cases as a function of flap deflection. The results indicate a steady increase in $C_{\lambda max}$ and a decrease in α_{stall} with increasing deflection.

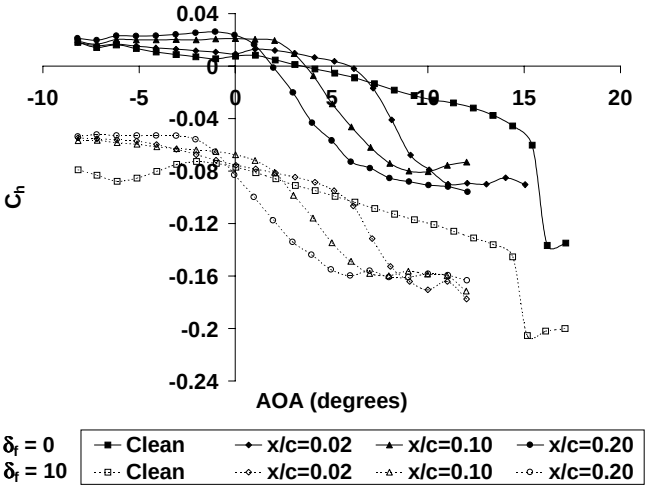

Fig. 4. Flap hinge moment for different simulated ice shape locations at Re = 1.8 million for δ_f = 0° and δ_f = 10°.

As seen from Figure 4, there is an obvious difference in the C_h at negative angles of attack for the clean case in comparison to that of the simulated-iced cases. Contrary to that at δ_f = 0°, the C_h curves do not diverge from the same value at negative angles of attack when δ_f = 10°. The C_h curve for the clean case has values that are lower in comparison. Figure 5 shows that this variation in the clean case at negative angles of attack increases with increasing flap deflection.

Table 3. $C_{\lambda max}$ and α_{stall} as a function of flap deflection and simulated ice shape location.

	$C_{l\ max}$				α_{stall}			
δ_f	Clean	.02	.10	.20	Clean	.02	.10	.20
0	1.5	.61	.40	.31	15.4°	8°	6°	6°
5	1.6	.73	.54	.44	14.4°	7°	5°	5°
10	1.7	.86	.64	.53	14.4°	6°	5°	4°
15	1.8	.97	.77	.73	14.4°	5°	3°	3°

A secondary effect resulting from the change in flap deflection exists and requires a brief identification of regions of the C_h curve. The first region is that occurring before the break in the curve, the second is the region of

rapidly decreasing C_h after the break, and the third is the leveling off of the curve to a constant C_h value at airfoil stall. The difference in value between the C_h at the end of the first region and that at which stall occurs decreases as the flap deflection increases. In other words, the range of C_h values in the second region decreases with increasing flap deflection. This is illustrated in Figure 5 showing the clean case at deflections of δ_f = 0°, 5°, 10° and 15°.

Furthermore, for the case of simulated ice at x/c = 0.20, there is a negative shift in the angle of attack at which the C_h curve breaks. As the flap is deflected in five-degree increments from δ_f = 0° to 15°, the angle of attack at which the curve breaks decreases by one-degree increments. For each of the other cases, the break shifts only one degree over the range of flap deflections.

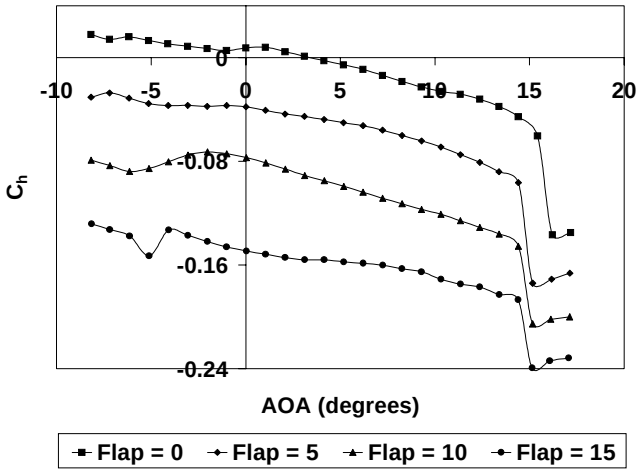

Fig. 5. Flap hinge moment at Re = 1.8 million for clean case at all flap deflections.

The unsteady hinge moment results are expressed in the form of the root mean square (RMS) of the C_h, expressed by the conventional definition,

$$C_{h,RMS} = \sqrt{\frac{1}{N}\sum \left(C_h - \overline{C_h}\right)^2}$$

where N represents the 10,000 C_h measurements taken. The $C_{h,RMS}$ is presented as a function of angle of attack and the break in the curve is determined by comparison with the clean case. A normalized parameter was calculated by considering the ratio of the iced $C_{h,RMS}$ value to the clean $C_{h,RMS}$ value at the same angle of attack. A significant break in the simulated-iced values from that of the clean case occurred when this normalized value was greater than 1.20.

Figure 6 shows the effects of the simulated ice on the RMS parameter. For the clean case, the $C_{h,RMS}$ remains fairly constant at a value of 0.004 until about α = 16°, where it increases sharply and then drops off again. The case of simulated ice at x/c = 0.02 has $C_{h,RMS}$ values that are nearly identical to those of the clean case until the curve begins to break at α = 5° where it exhibits the same rising and falling trend. Similarly, when the simulated ice is located at x/c = 0.10 and x/c = 0.20, the $C_{h,RMS}$ breaks at α = -3° and α = -4°, respectively. The range of angles of attack corresponding to the maximum values of $C_{h,RMS}$ increases when considering first the clean case, and then the simulated-iced cases in order of increasing x/c. The slopes of the rising portions of the curves decrease in value according to this same trend.

Figure 6 illustrates the effect of a 10° flap deflection on the unsteady hinge moment. The $C_{h,RMS}$ curves shift toward decreasing angle of attack and exhibit a slight decrease in the maximum value. In addition, the breaks in the $C_{h,RMS}$ curves occur approximately one degree prior to those in the case of no flap deflection.

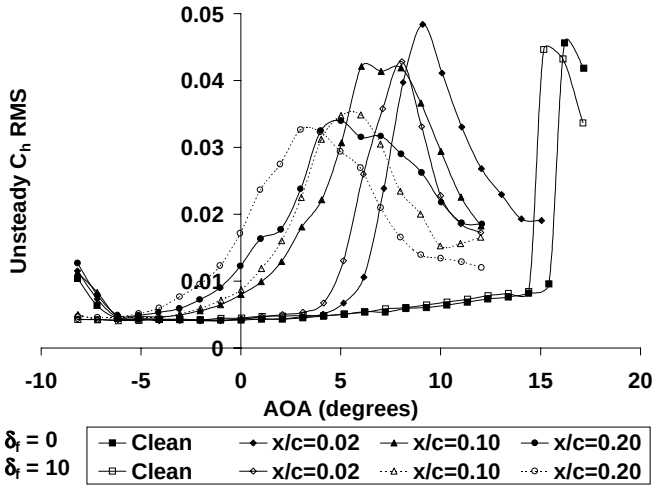

Fig. 6. Unsteady flap hinge moment at Re = 1.8 million for δ_f = 0° and δ_f = 10°.

3.3 Correlation of C_h with Lift and Drag

Trends in the lift and drag coefficients can be compared with those of the steady and unsteady hinge moment coefficients. Figure 7 shows the C_h and $C_{h,RMS}$ curves with arrows that denote significant angles of attack with regard to the lift and drag curves. The upward-pointing arrows mark the angles at which $C_{\lambda max}$ occurs, Table 3, and the downward-pointing arrows represent the nonlinear breaks in the drag buckets.

Figure 7a illustrates the results for the steady-state hinge moment and shows that $C_{\lambda max}$ occurs after the break in the C_h curve. For the clean case, stall occurs abruptly following a complete separation of the flow over

the airfoil, thus the maximum lift and the break in the hinge moment occur simultaneously. On the other hand, the stalling process of the simulated-iced cases is more gradual. With the quarter round at x/c = 0.02 and x/c = 0.10, the break in the C_h curve occurs 1° and 3°, respectively, before $C_{\lambda max}$ is reached. For the x/c = 0.20 case, the difference is approximately 5°.

For the drag comparison, the nonlinear breaks in the C_d, defined earlier in reference to Figure 3b, occur in the linear region of the C_h curves. The difference in angle of attack between the breaks in the C_d and C_h tends to decrease as the quarter round moves downstream.

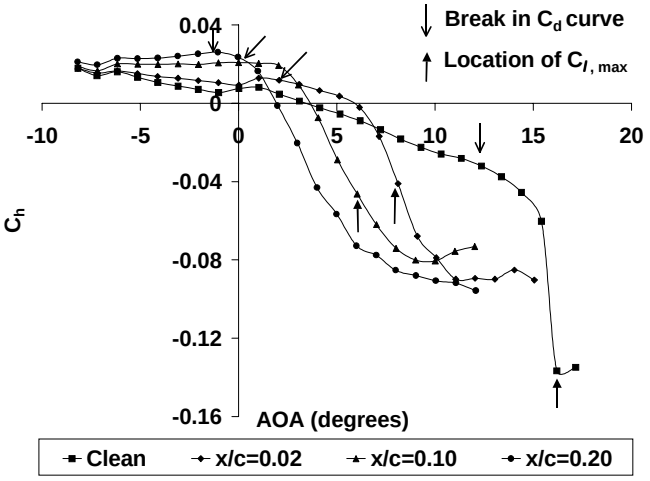

Fig. 7a. Correlation of C_h with $C_{\lambda max}$ and C_d nonlinearity at Re = 1.8 million for various simulated ice shape locations, δ_f = 0°.

The lift and drag comparisons with the unsteady hinge moment are shown in Figure 7b. For the clean case, $C_{\lambda max}$ occurs at the angle of attack prior to the rapid increase in the $C_{h,RMS}$, again due to the abrupt stalling mechanism. For the cases with simulated ice at x/c = 0.02 and x/c = 0.10, $C_{\lambda max}$ occurs at or near the maximum $C_{h,RMS}$ value. The breaks in the drag curves for the clean and x/c = 0.02 simulated-iced cases occur in the linear $C_{h,RMS}$ range. There is a 4° difference between the C_d and $C_{h,RMS}$ breaks for the clean airfoil, and a 3° difference for the iced airfoil. For the remaining two cases with simulated ice, the break in the C_d occurred after the break in the $C_{h,RMS}$, with a difference of 4° in both cases.

Further comparison can be made between the nonlinearities in the hinge moment and lift results. In each case, the steady-state C_h breaks at an angle of attack corresponding to the nonlinear range of the lift curve. For

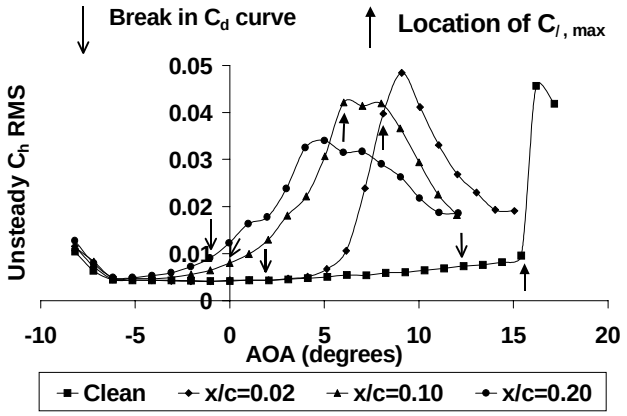

Fig. 7b. Correlation of unsteady $C_{h,RMS}$ with $C_{\lambda max}$ and C_d nonlinearity at Re = 1.8 million for various simulated ice shape location, δ_f = 0°.

the clean airfoil the C_h breaks at α_{stall}, while for the simulated-iced cases it breaks at the point in which the rate of increase of lift begins to decline slightly, where the lift curve rounds over. The unsteady parameter tends to break at lower angles, especially when the quarter round is located further back on the airfoil. The $C_{h,RMS}$ breaks at the same angle of attack as the C_h for the clean case. With simulated ice, however, the $C_{h,RMS}$ breaks in the linear range of the lift curve. The result of this is that the $C_{h,RMS}$ parameter provides several degrees of warning that flow separation is approaching if the angle of attack continues to be increased. Table 4 provides values for each of these trends.

Table 4. Comparison of angles of attack in correlation with C_h and $C_{h,RMS}$.

Test Case	α_{stall}	C_h break	$C_{h,RMS}$ break
Clean	15.4°	15.4°	15.4°
x/c = 0.02	8°	7°	5°
x/c = 0.10	6°	3°	-3°
x/c = 0.20	6°	1°	-4°

3.4 Flowfield Analysis

Fluorescent oil flow visualization was performed in order to understand better the results of the previous section. The boundary layer state as a function of angle of attack, from α = 0° to α = 5°, is mapped in Figure 8. The Reynolds number was 1.8 million and the simulated ice shape was placed at the x/c = 0.10 location.

Two separation bubbles, one upstream and one downstream of the quarter round, were observed on the

surface of the airfoil. At $\alpha = 0°$ a small separation bubble was located between x/c = 0.07 and x/c = 0.10 and moved forward with angle of attack to x/c = 0.05 at $\alpha = 3°$. The bubble prevailed at this location for the remaining angles. The larger bubble formed aft of the quarter round and reattached between x/c = 0.40 and x/c = 0.44 at $\alpha = 0°$. This region was not clearly defined because the reattachment of the ice-induced bubble was seen as a band of relatively stagnant oil on the surface. The reattachment zone gradually moved downstream with increasing angle of attack, fluctuating somewhat in size, until reaching the flap (x/c = 0.75) at $\alpha = 3°$. This is reflected in Figure 4 where the break in the C_h curve occurs. The reattachment zone continued to move downstream, extending to the trailing edge at $\alpha = 3.5°$. The rapid growth of the separation bubble, characteristic of a thin airfoil stall, confirmed the results illustrated by the lift curves.

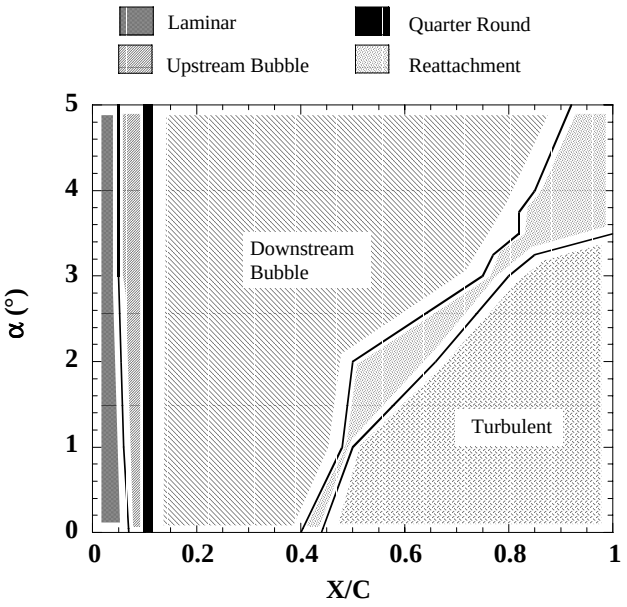

Fig. 8. Summary of boundary-layer state with 0.25-inch simulated ice shape at x/c = 0.10 obtained from oil flow visualization at Re = 1.8 million.

The large change in the flowfield around the airfoil can be seen in the pressure distribution plots of Figure 9. It is important to note that the surface pressure was not measured at the position of the simulated ice shape. Thus, these C_p data points are not present in the pressure distribution curves. Furthermore, there is a discontinuity in the C_p at x/c = 0.78 due to the flap gap.

Figure 9a shows a comparison of the surface pressure distributions for the clean and simulated-iced airfoils at $\alpha = 0°$. The clean case shows the stagnation point at the leading edge with a suction peak at x/c = 0.12 on the upper surface. When the quarter round was located at x/c = 0.02, the flow accelerated over it and separated, producing a large suction peak immediately downstream of the simulated ice. Since the simulated ice shape coincided with a very favorable pressure gradient, the bubble quickly reattached at x/c = 0.10. This allowed another suction peak (due to the airfoil geometry and not the simulated ice shape) to form at x/c = 0.16 with a value lower than that of the clean model.

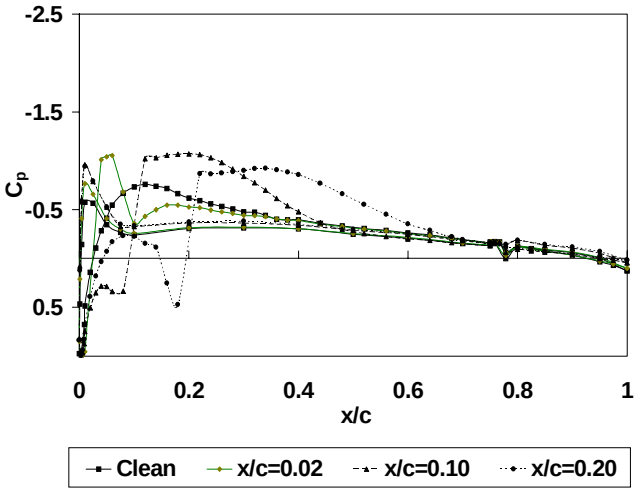

Fig. 9a. Surface pressure distribution for various simulated ice shape locations at $\alpha = 0°$, Re = 1.8 million, $\delta_f = 0$.

With the ice accretion at x/c = 0.10, the flow on the upper surface initially accelerated from the leading-edge stagnation point but then decelerated as it approached the quarter round. This occurred because of an adverse pressure gradient that caused the flow to separate, resulting in a local minimum and maximum pressure. Immediately downstream of the quarter round, a longer separation bubble formed, and the C_p was nearly constant until x/c = 0.24, where it started to increase as the reattachment process began. The presence of the separation bubble in an adverse pressure gradient prolonged reattachment until approximately x/c = 0.44. This pressure distribution is reconfirmed by the flow visualization results presented in Figure 8.

When the simulated ice shape was moved downstream to x/c = 0.20, the flow was able to accelerate before the ice shape and obtain a local minimum pressure of notable magnitude. Since both the simulated ice shape and the separation bubble were located in an adverse pressure gradient, the size of the bubble was greater compared to the previous case, extending to x/c = 0.68.

Similar trends for the surface pressure distribution at $\alpha = 5°$ are shown in Figure 9b. The suction peak for the clean case occurs at x/c = 0.08. When the simulated ice

shape was placed at x/c = 0.02, the flow separated and produced a pressure peak of lower pressure than the clean case suction peak, at the same location. The pressure distribution over the remainder of the airfoil resembles but never quite matches that of the clean case. For the case of simulated ice at x/c = 0.10, a local minimum is observed as in the $\alpha = 0°$ case, but of greater magnitude. Although the separation bubble exhibits the same pressure at both angles, the flow at $\alpha = 5°$ never recovers. This corresponds with the flow visualization summarized in Figure 8 where the reattachment zone extends all the way to the trailing edge. This complete flow separation occurs with the quarter round at x/c = 0.20 as well. While the pressure of the separation bubble is slightly higher at $\alpha = 5°$ than at $\alpha = 0°$, the upstream suction peak is lower.

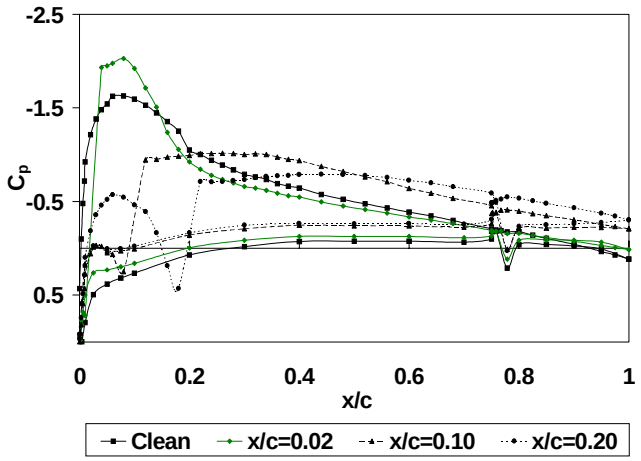

Fig. 9b. Surface pressure distribution for various simulated ice shape locations at $\alpha = 5°$, Re = 1.8 million, $\delta_f = 0$.

On a clean NACA 23012, more than 50% of the lift is generated in the first quarter chord of the airfoil. Thus, the location and size of both the suction peak and the separation bubble play an important role in determining the amount of lift that is produced on an iced airfoil. Lee and Bragg[10] studied additional locations of simulated ice and observed that long separation bubbles formed when the simulated ice shape was near the clean airfoil suction peak in the pressure recovery region. The unfavorable pressure gradient prolonged bubble reattachment and eliminated the suction peak on the clean airfoil. Furthermore the largest loss in lift occurred when the 0.25-inch simulated ice shape was located just upstream of the maximum adverse pressure gradient. When the simulated ice shape was located far enough downstream, however, a small local suction peak was able to form upstream of the simulated ice shape, recovering some of the lift.

Examination of the pressure distributions over the flap provides insight into the C_h trends illustrated earlier. From Figure 10a, it is observed that the C_p values of the clean case and the case of simulated ice at x/c = 0.02 closely resemble each other, as do the iced cases at x/c = 0.10 and x/c = 0.20. This is also evident by their similar C_h values at $\alpha = 0°$ in Figure 4. In each case, the pressure acting on the upper surface of the airfoil is greater than that on the lower surface resulting in a downward force on the flap and a positive hinge moment coefficient. Note that the fewer number of data points on the flap lower surface distinguishes it from the upper surface.

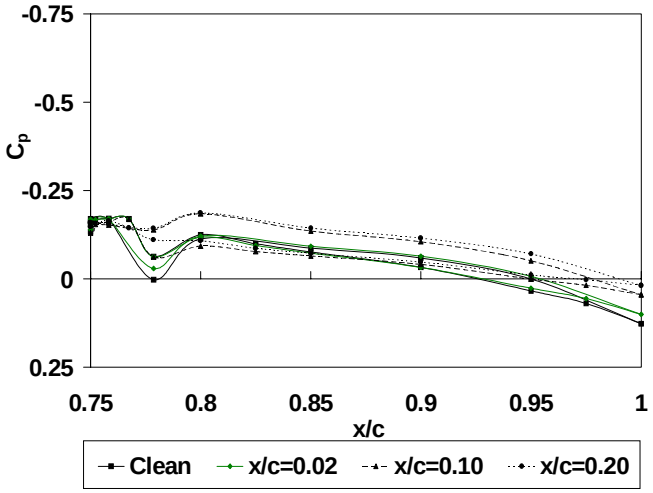

Fig. 10a. Flap surface pressure distribution for various simulated ice shape locations at $\alpha = 0°$, Re = 1.8 million, $\delta_f = 0$.

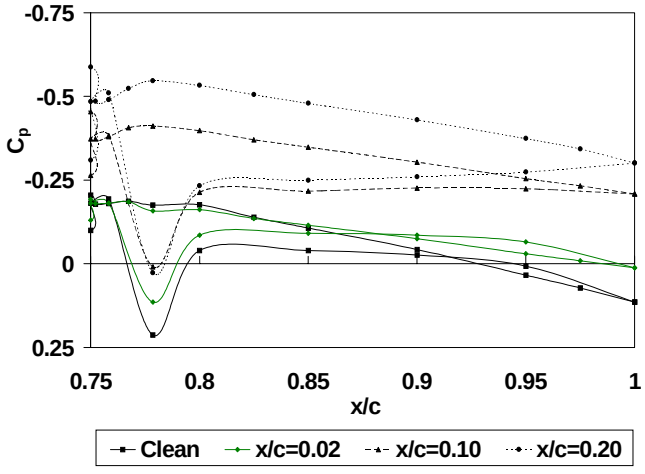

Fig. 10b. Flap surface pressure distribution for various simulated ice shape locations at $\alpha = 5°$, Re = 1.8 million, $\delta_f = 0$.

Figure 10b shows the flap pressure distribution at α = 5°. For the clean case, the pressure acting near the flap hinge line is greater on the lower surface side. As the trailing edge of the flap is approached the distribution changes such that the pressure acting on the upper surface is greater. The opposing moments result in a net upward force and thus a negative C_h value near zero. A similar transition occurs when the simulated ice shape is at x/c = 0.02, except that in this case the resultant force acts downward and C_h is positive. For the remaining two quarter round locations, the flow is completely separated, resulting in decreased pressure over the flap upper surface, creating an upward force and a negative C_h. The difference between the upper and lower pressure distributions is greater when the quarter round is located at x/c = 0.20, thus C_h is more negative at this position.

Further analysis of the pressure distribution over the flap indicates a correlation between the angle of attack at which the bubble reaches the flap and the angle at which the hinge moment coefficient breaks. For each of the clean and simulated-iced airfoils, these two phenomena occur at the same angles of attack, those being 16°, 7°, 3° and 1° respectively for the clean and simulated-iced cases.

Figures 11a and 11b show the pressure distributions over the airfoil when the simulated ice shape is at x/c = 0.10 and the angle of attack ranges from α = 0° to 5°. For α = 0°, 1° and 2°, the upper surface of the airfoil experiences a greater pressure distribution, resulting in fairly constant positive C_h values. At α = 3° and 4°, the pressure acting on the lower surface increases until finally at α = 5° the entire lower surface pressure distribution is less than that acting on the upper surface and the C_h becomes a negative value. Note that the transition of the more positive pressure distribution from the upper to the lower flap surface occurs between the same angles of attack that the hinge moment coefficient passes through zero. This further coincides with the location at which the reattachment zone extends to the trailing edge in the oil flow visualization. In addition, the pressure distribution over the flap changes significantly between α = 2° and α = 3° when the separation bubble reaches the flap. These large changes in pressure continue as angle of attack is increased and the flow over the flap completely separates.

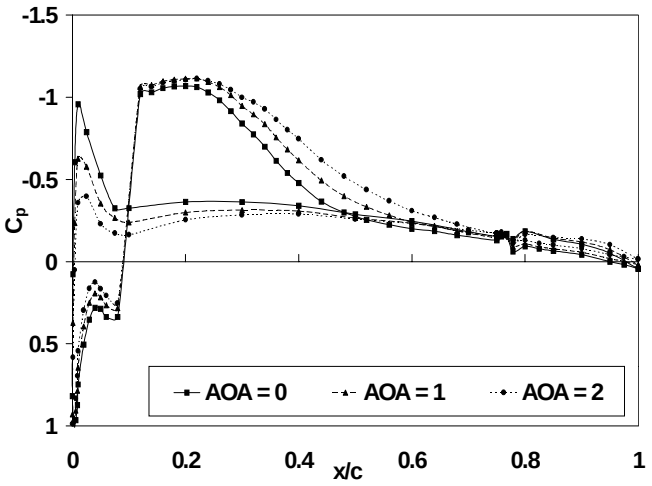

Fig. 11a. Surface pressure distribution with simulated ice shape at x/c = 0.10, Re = 1.8 million, and δ_f = 0.

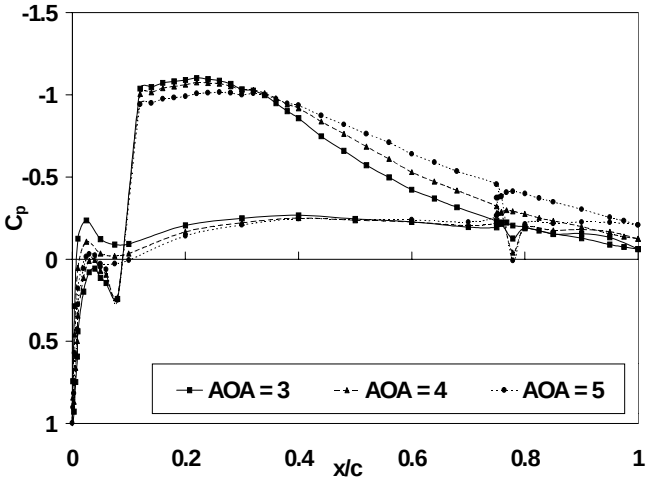

Fig. 11b. Surface pressure distribution with simulated ice shape at x/c = 0.10, Re = 1.8 million, and δ_f = 0.

Figure 12 shows the effect of increasing flap deflection on the surface pressure distribution at a fixed simulated ice shape location and at constant angle of attack. The Cp curves become more negative on the upper surface and more positive on the lower surface during the 15° flap variation. This explains the trends with flap deflection seen in Figures 4 and 5.

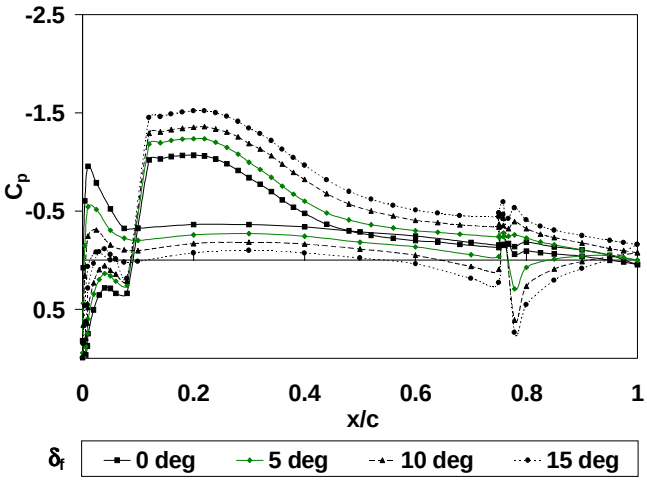

Fig. 12. Surface pressure distribution for various flap deflections with simulated ice shape at x/c = 0.10, Re = 1.8 million, and $\alpha = 0°$.

4.0 Summary

The presence of simulated ice on a NACA 23012 airfoil produced reduced lift, increased drag and changes in pitching moment. These resulted from a separation bubble that formed behind the simulated ice, severely altering the surface pressure distribution. The steady-state hinge moment became nonlinear when flow separation occurred over the flap and was most affected when the simulated ice was located furthest aft on the upper surface. The fluctuation of the flap hinge moment was characterized by a RMS parameter that exhibited a maximum value at or near maximum lift. As opposed to the steady-state value, the change in the RMS hinge moment was observed during the linear phase of the lift curve. This supports the possibility of using the unsteady flap hinge moment as a sensor of oncoming ice-induced aircraft control problems.

5.0 Acknowledgment

This work was supported in part by a Critical Research Initiatives grant from the University of Illinois. The authors would like to thank Sam Lee and Andy Broeren for their assistance in the acquisition and reduction of the wind tunnel data. Han Kim assisted in the preparation of this document.

The ice accretion sensor concept described in this paper is the basis of an ongoing patent application by the authors.

[1] Bragg, M.B., Perkins, W.R., Sarter, N.B., Basar, T., Voulgaris, P.G., Gurbacki, H.M., Melody, J.W., McCray, S.A., "An Interdisciplinary Approach to In-flight Aircraft Icing Safety," AIAA Paper 98-0095, Reno, NV, 1998.

[2] Trunov, O.K. and Ingelman-Sundberg, M., "On the Problem of Horizontal Tail Stall Due to Ice," The Swedish-Soviet Working Group on Scientific-Technical Cooperation in the Field of Flight Safety, Report No. JR-3, 1985.

[3] Johnson, C.L., "Wing Loading, Icing and Associated Aspects of Modern Transport Design," *Journal of the Aeronautical Sciences*, vol. 8, no. 2, December 1940, pp. 43-54.

[4] Bragg, M.B., "Aircraft Aerodynamic Effects due to Large Droplet Ice Accretions," AIAA Paper 96-0932, Reno, NV, 1996.

[5] Pruzan, D.A., Khatkhate, A.A., Gerardi, J.J., Hickman, G.A., "Smart Skin Technology Development for Measuring Ice Accretion, Stall, and High AOA Aircraft Performance, Final Technical Report, Part 2, Surface Pressure Separation/Stall Detector Development," NASA Contract No. NAS3-25966, Report No. 93D-03-0423, April 23, 1993.

[6] Maris, J.M., "Airfoil Performance Monitoring using the Turbulence Intensity Parameter," Proceedings of the FAA International Conference on Aircraft In-flight Icing, Vol. II, Working Group Papers, Final Report, August, 1996.

[7] Cronin, D., Vogel, J., and Lamb, M., "Analytical Development and Experimental Results of a Method for Aerodynamic Contamination Detection," International Icing Symposium '95, September 18-21, 1995.

[8] Rae, W. H. and Pope, A., *Low-Speed Wind Tunnel Testing*, John Wiley & Sons, 1984.

[9] Althaus, D. and Wortmann, F. "Experimental Results from the Laminar Wind Tunnel of the Institute for Aerodynamic and Gasdynamics - The University of Stuttgart" published by Princeton University, Department of Mechanical and Aerospace Engineering, 1979.

[10] Lee, S., Dunn, T., Gurbacki, H. M., Bragg, M. B., and Loth, E., "An Experimental and Computational Investigation of Spanwise-Step-Ice Shapes on Airfoil Aerodynamics", AIAA 98-0490, January, 1998.